RESEARCH ARTICLE | JANUARY 06 2025

Interlayer and intralayer magnetic interactions for room-temperature strong ferrimagnetism of layered organic–inorganic hybrid nanoplates

Qifeng Kuang; Bo Zhang; Baojuan Dong; Xiaoling Men; Bing Yang ; Yangtao Zhou ; Zhiwei Li ; Xiaolei Shang ; Teng Yang ; Jianqi Huang ; Da Li ; Zhidong Zhang

J. Appl. Phys. 137, 013908 (2025)
https://doi.org/10.1063/5.0237015

Journal of Applied Physics ARTICLE pubs.aip.org/aip/jap

Interlayer and intralayer magnetic interactions for room-temperature strong ferrimagnetism of layered organic–inorganic hybrid nanoplates

Cite as: J. Appl. Phys. **137**, 013908 (2025); doi: 10.1063/5.0237015
Submitted: 21 November 2024 · Accepted: 19 December 2024 ·
Published Online: 6 January 2025

Qifeng Kuang,[1,2] Bo Zhang,[3] Baojuan Dong,[4] Xiaoling Men,[1,2] Bing Yang,[1] Yangtao Zhou,[1] Zhiwei Li,[3] Xiaolei Shang,[1] Teng Yang,[1] Jianqi Huang,[1,5,a)] Da Li,[1,2,b] and Zhidong Zhang[1]

AFFILIATIONS

[1]Shenyang National Laboratory for Materials Science, Institute of Metal Research, Chinese Academy of Sciences, Shenyang 110016, China
[2]School of Materials Science and Engineering, University of Science and Technology of China, Shenyang 110016, China
[3]School of Physical Science and Technology, Lanzhou University, Lanzhou 730000, China
[4]College Physics and Electronic Engineering, Shanxi University, Taiyuan 030006, China
[5]Liaoning Academy of Materials, Shenyang 110167, China

[a)]**E-mail:** jqhuang@lam.ln.cn
[b)]**Author to whom correspondence should be addressed:** dali@imr.ac.cn

ABSTRACT

In the past few decades, a development of organic magnets with room-temperature strong ferromagnetism is challenged by the difficulty of creating three-dimensional (3D) long-range magnetic orderings in organic materials at a temperature higher than room temperature. Here, we report room-temperature ferrimagnetism of a tetragonal organic–inorganic hybrid $Fe_{14}Se_{16}(tepa)_{III}$ (tepa = tetraethylenepentamine), where III represents a coordination of a tepa molecule with a Fe^{3+} ion for an organic complex. The layered hybrid in a nanoplate-like shape is formed by periodic incorporation of tetragonal β-Fe_3Se_4 inorganic layers and organic spacing layers consisting of tepa and Fe^{3+}. $Fe_{14}Se_{16}(tepa)_{III}$ shows a saturation magnetization M_S of 7.2 emu g^{-1} at 300 K and a record-high Néel temperature T_N (>560 K) in the organic magnets reported experimentally. A Mössbauer spectrum confirms a 3D long-range magnetic ordering of Fe^{2+} [$S = 2$ (71.4%)] and Fe^{3+} ions [$S = 5/2$ (21.7%) and 1/2 (4.0%)] in β-Fe_3Se_4 layers and organic spacing layers of $Fe_{14}Se_{16}(tepa)_{III,9}$. First-principles calculations explain that the 3D long-range antiferromagnetic interactions between interlayer and intralayer irons result in the strong ferrimagnetism of $Fe_{14}Se_{16}(tepa)_{III}$. This study unveils the possibility of tuning magnetic couplings of interlayer and intralayer high-spin Fe^{3+} and Fe^{2+} for enhancing the ferrimagnetism of layered hybrids and, thus, for future room-temperature magnetic/spintronic applications.

I. INTRODUCTION

A rapid increase of demand in next-generation magnets leads to impressive progresses in advanced magnets through introduction of novel concepts and discovery of new materials. Organic magnetic materials, such as molecular magnets, magnetic organometallic frameworks (MOFs), and organic–inorganic hybrid magnets, comprised in part or wholly of molecular components, are potential for future multifunctional applications due to excellent electronic, optical, magnetic, and mechanical properties and low density.[1–5] Magnetic interactions between magnetic units play an important role in the magnetism of organic magnets, particularly magnetic-ordering temperatures. In the case of molecule-based magnets, a strategy to raise the magnetic-ordering temperature is to utilize strong magnetic couplings between radical-based ligands, such as an $S = 1/2$ tetracyanoethylene radical ($[TCNE]^{\bullet-}$) and transition metals, for example, $V(TCNE)_x{\cdot}y(CH_2Cl_2)$ ($x \sim 2$, $y \sim 1/2$)

generating a magnetically ordered phase with a Curie temperature T_C exceeding its thermal decomposition temperature (T_d) of 350 K,[6] while $V[Cr(CN)_6]_{0.86}\cdot 2.8H_2O$ exhibits ferrimagnetism with $T_N = 315$ K arising from uncompensated spins of Cr^{3+} and V^{3+} ions with long-range antiferromagnetic (AFM) interactions.[7] The $K_{0.058}V^{2+/3+}[Cr^{3+}(CN)_6]_{0.79}\cdot(SO_4)_{0.058}\cdot 0.93H_2O$ shows excellent air stability and the T_C value of ~373 K owing to the larger radial extension of V^{2+} d-orbitals, resulting in an improved orbital overlap and consequently an enhanced magnetic exchange.[8] Recently, redox-active radical ligands were incorporated into MOFs, leading to strong magnetic interactions.[9,10] Among them, $Li_{0.7}[Cr(pyrazine)_4]Cl_{0.7}\cdot 0.25THF$ exhibits ferrimagnetic (FIM) ordering up to 515 K,[10] despite long distances between metal centers. Organic–inorganic hybrids not only integrate excellent characteristics of inorganic and organic materials and nanomaterials, but also produce new properties differing from their constituent units, providing a favorable material basis for a multifunction.[11,12] The periodic incorporation of inorganic fragments and organic ligands/complexes in a single lattice provides additional tuning capabilities for the magnetism of ordered organic–inorganic hybrids.[13–15]

Because the constituent elements of C, H, O, and N in organic ligands merely contain s or p electrons, the spatial separation of inorganic fragments by organic ligands/complexes rarely creates organic–inorganic hybrids in a room-temperature long-range magnetic order. The spins of magnetic ions are usually AFM coupled in organic magnets due to the indirect exchange coupling through coordinated organic linkers. Most of the organic magnets exhibit weak magnetizations (<1 emu g^{-1}) at 300 K. From the application perspective, organic magnets with high saturation magnetization (M_S) and a high magnetic-ordering temperature are fascinating. In addition to small amounts of molecular magnets/MOFs,[6–8,10,16] to our best knowledge, there have been rare reports on the ordered organic–inorganic hybrid magnets with their magnetic-ordering temperatures near or higher than 300 K.[17,18] The $(\beta\text{-}Fe_3Se_4)_4[Fe(teta)_{1.5}]$ (teta = triethylenetetramine) shows the highest magnetic ordering (>530 K) among the reported organic–inorganic hybrid magnets.[17] Several theoretical and experimental studies were performed by tuning organic ligands and magnetic ions/fragments to enhance the magnetic properties of organic magnets.[18–21] However, challenges still remain in the discovery of organic magnets with room-temperature strong ferromagnetism.

Different magnetic organic–inorganic hybrids were synthesized by combination of various inorganic Fe_xSe (x = 1/2, 2/3, and 3/4) superstructures with varied organic Fe^{2+}-amine complexes [amine = en (ethylenediamine), dien (diethylenetriamine), tren (tris(2-aminoethyl)amine), teta, and tepa].[17,18,21–23] $Fe_{14}Se_{16}$(tepa) nanoplates exhibit room-temperature ferrimagnetism with the highest value for a saturation magnetization of $M_S = 4$ emu g^{-1} at 300 K.[24] From a crystallographic perspective, tepa-coordinated and uncoordinated irons in organic spacer layers may, respectively, occupy the 2*b* and 2*a* sites of tetragonal $Fe_{14}Se_{16}$(tepa) with the space group *I*4/*mmm*.[24] An immediate question arises as what results in the strong magnetism and whether a stronger magnetism can be obtained by using high-spin Fe^{3+} replacing Fe^{2+} in organic spacer layers of $Fe_{14}Se_{16}$(tepa). Here, we define hybrid nanoplates consisting of inorganic Fe_3Se_4 layers and organic tepa/Fe^{2+} spacer layers as $Fe_{14}Se_{16}(tepa)_{II}$.

In this article, we report synthesis and magnetic properties of $Fe_{14}Se_{16}(tepa)_{III}$ with an M_S value up to 7.2 emu g^{-1} at 300 K and a record-high Néel temperature ($T_N > 560$ K). Varied oxidation/spin states and occupations of irons are revealed by Mössbauer results. First-principles calculations and Mössbauer analysis reveal that strong FIM properties of $Fe_{14}Se_{16}(tepa)_{III}$ originate from a 3D long-range AFM interaction of interlayer and the intralayer high-spin Fe^{3+} and Fe^{2+} ions in the hybrid lattice.

II. EXPERIMENTAL

$Fe_{14}Se_{16}(tepa)_{III,t}$ hybrid nanoplates were synthesized by diffusing Fe^{3+} ions into a hybrid precursor $(\beta\text{-}Fe_2Se_3)_4[Fe(tepa)]$ at a reaction temperature of 453 K with a reaction time *t* in a two-step route as described elsewhere.[24] Effects of *t* on the composition, structure, and magnetism of hybrids are summarized in Table S1 of the supplementary material. The $Fe_{14}Se_{16}(tepa)_{III,9}$ with the largest room-temperature M_S value will be focused on below.

Powder X-ray diffraction (XRD) measurements were performed using a D/Max-2400 diffractometer (Rigaku, Inc., Tokyo, Japan) equipped with a Cu Kα ($\lambda = 0.154056$ nm) radiation source at room temperature. The program Rietica was used to refine the crystal structure of the hybrid products. For the refinements, the XRD data were obtained at a slow scanning rate of 1° min^{-1} with a step size of 0.01°. *In situ* high-temperature XRD data were obtained on a Bruker D8 Advance diffractometer configured with a molybdenum (Mo) heater as the stage for the powder samples, in which the data were collected by *in situ* heating the samples in a temperature range between 300 and 750 K under vacuum. The Mo heater was characterized by the XRD peaks at $2\theta = 40.56°$ and 58.61°, respectively, corresponding to the (110) and (200) diffraction planes. The size and morphology of the hybrids were examined by a JSM 6301F field-emission scanning electron microscope (FESEM) (JEOL, Inc., Tokyo, Japan) system. Elemental compositions of the hybrids were analyzed by Oxford energy dispersive X-ray (EDX) spectroscopy. Transmission electron microscopy (TEM), a selected area electron diffraction (SAED) pattern, and scanning transmission electron microscopy (STEM) images were taken on a Tecnai G2 F20 microscope (FEI, Inc., Hillsboro, OR, USA) operated at an acceleration voltage of 200 kV. The specimens were prepared by evaporating a drop of dilute solution of hybrids dispersed in absolute ethanol on an amorphous carbon–copper grid. A Fourier transform infrared (FTIR) spectrum was recorded on a Nicolet iN10 MX and iS10 spectrometer using the KBr pellet technique (Thermo Fisher, Inc., Waltham, MA, USA). Thermal gravimetric analysis (TGA) was carried out on a STA6000 thermal analyzer (PerkinElmer, Inc., Waltham, MA, USA) with a heating rate of 10 K min^{-1} between 300 and 800 K. Soft Fe L-edge X-ray absorption spectrum (XAS) measurements were performed at BL08U1A of the Shanghai Synchrotron Radiation Facility (SSRF) in the total electron yield (TEY) mode at room temperature. Fe L-edge spectra consist of sharp peaks around 709 eV (L_3 edge) and 720 eV (L_2 edge), resulting from the spin–orbit splitting of the core levels. The background vacuum level was 1×10^{-9} Torr. The powder sample was pasted on a Cu conducting tape, and the angle between the incident synchrotron radiation and the tape is 90°. Scans were collected in 0.1 eV steps and a 700–735 eV energy scale. ^{57}Fe

Mössbauer spectra were recorded by a conventional constant acceleration spectrometer operated in a multi-channel scaling mode at 5 K. The spectrometer was calibrated by a 25 μm thick natural abundance α-Fe foil. The isomer shifts were determined relative to that of α-Fe. The fitting was performed by the least squares method in the MossWinn software.

Magnetic measurements were conducted using a vibrating sample magnetometer (VSM) standard option in a physical property measurement system (PPMS) equipped with a superconducting magnet with a maximum magnetic field of 140 kOe. Temperature-dependent magnetization measurements were recorded in dc fields ($H = 0.1$ and 50 kOe) in a temperature range 10–300 K after cooling in zero-field cooled (ZFC) and field cooled (FC) modes. Static magnetic measurements were performed in a dc field range between −50 and 50 kOe and a temperature range from 10 to 500 K. The data were collected by using the standard VSM mode in the temperature range between 10 and 300 K and by using the oven mode in a high vacuum state with a chamber pressure lower than 1×10^{-5} Torr between 300 and 750 K.

First-principles calculations were constructed on a simplified structural model with the space group *I*4/*mmm* for $Fe_{14}Se_{16}(tepa)_{III,9}$.[24] Specifically, we maintained the atomic structure of an inorganic β-Fe_3Se_4 layer, while simplified an organic spacer layer to include only Fe atoms since we concentrated on the magnetic study herein with negligible magnetic moments of C, N, and H atoms. There are two kinds of Fe atoms in an organic spacer layer, designated as Fe1 and Fe2. Fe2 is situated at the Wyckoff position 2b (0, 0, 1/2; 1/2, 1/2, 0) of the space group *I*4/*mmm*,[24] where it coordinates with a tepa molecule in the form of a Fe(tepa) complex. In contrast, Fe1 is located in an interstitial space among Fe(tepa) complexes, occupying the Wyckoff position 2a (0, 0, 0; 1/2, 1/2, 1/2). First-principles calculations based on density functional theory (DFT) were performed using the generalized gradient approximation (GGA) with Perdew–Burke–Ernzerhof functional, as implemented in the Vienna *ab initio* simulation package (VASP).[25,26] The projected augmented wave (PAW) method with a plane-wave basis set was used with a cutoff energy of 500 eV.[27] A Monkhorst–Pack k mesh of $6 \times 6 \times 4$ was adopted to represent the first Brillouin zone of the reciprocal space.[28] The lattice constants of experimental values were fixed in the calculation, and only atomic positions were relaxed by the conjugated gradient method. The convergence criteria for the energy and force were set to 10^{-5} eV and 0.01 eV Å^{-1}, respectively.

III. RESULTS AND DISCUSSION

FESEM [Fig. 1(a)] and TEM [Fig. 1(b)] images show a nanoplate-like shape of $Fe_{14}Se_{16}(tepa)_{III,9}$ with a thickness ranging from 100 to 200 nm and a length of 0.3–5 μm. An EDX spectrum in Fig. 1(c) indicates the presence of Fe, Se, Cu, C, and N elements in $Fe_{14}Se_{16}(tepa)_{III,9}$. Among them, the Cu element comes from a copper conductive tape, and thus, Fe and Se are the only heavy elements in the hybrid nanoplates. A relative molar ratio of Fe to Se in $Fe_{14}Se_{16}(tepa)_{III,9}$ is determined to be 46.31/53.69 (6.90/8) by EDX, much close to the feed ratio and the value determined by an inductively coupled plasma (ICP) technique. Similar morphology and chemical compositions are observed in $Fe_{14}Se_{16}(tepa)_{III,3}$ and $Fe_{14}Se_{16}(tepa)_{III,12}$ (Figs. S1 and S2 in the supplementary material). An SAED pattern in Fig. 1(d) taken perpendicular to a hybrid nanoplate [Fig. 1(b)] reveals a single crystal-like lattice of $Fe_{14}Se_{16}(tepa)_{III,9}$ nanoplates with the tetragonal symmetry along the [001] direction. The $\sqrt{2} \times \sqrt{2}$ of Fe vacancy order is exactly the same as the ones found in tetragonal β-Fe_3Se_4 superstructures along the *c* direction.[29,30] Such a *c* axis zone pattern of β-Fe_3Se_4 is similar to that of superconducting β-FeSe, except that the systematic absences in (*h*00), (0*k*0), *h* odd, *k* odd, are now visible.[31] SAED patterns of $Fe_{14}Se_{16}(tepa)_{III,t}$ in Fig. S2 of the supplementary material indicate a high affinity of tetragonal structures with inorganic β-Fe_3Se_4 layers. A FTIR spectrum in Fig. 1(e) presents the stretching (ν)/bending (δ) vibration bands of $-CH_2-$, $-NH_2$, and –CN– that come from tepa in $Fe_{14}Se_{16}(tepa)_{III,9}$. X-ray absorption spectroscopy [Fig. 1(f)] shows the presence of both ferric and ferrous irons in the hybrid nanoplates. Commercial Fe_3O_4 is used as a reference revealing the oxidation states of Fe^{3+} and Fe^{2+}. A dependence of a hybrid structure on constitutional units was reported in previous compounds containing Fe_3Se_4 layers,[30] Fe_4Se_5 layers,[32] and FeSe/FeS layers.[33–35] Based on the electrical neutrality principles and a molar ratio between inorganic (Fe_7Se_8) and organic (tepa) components (Figs. S3–S4 in the supplementary material), a chemical formula of $(Fe^{2+}_{2.5}Fe^{3+}_{0.5}Se^{2-}_4)_4[Fe^{3+}(tepa)]Fe^{3+}$ is suggested for $Fe_{14}Se_{16}(tepa)_{III,9}$.

Figure 2(a) represents a slow scanning XRD pattern of $Fe_{14}Se_{16}(tepa)_{III,9}$ hybrid nanoplates recorded at room temperature. Two strong peaks at low 2θ angles of 9.15° and 18.32° with lattice spacings of 9.66 and 4.84 Å reveal the presence of periodic inorganic layers separated by organic spacer layers. Except for tiny Fe_3O_4 featured by a weak intensity of (311) around 35.4°, other Bragg diffraction peaks can be well indexed by the TEROR method using program Powder X,[36] suggesting a tetragonal crystal structure in the space group *I*4/*mmm* (No. 139) the same as the observation from the SAED [Fig. 1(d)]. The corresponding refinement process gives good *R* factors ($R_p = 8.45\%$, $R_{wp} = 10.1\%$, and $\chi^2 = 4.14$) for $Fe_{14}Se_{16}(tepa)_{III,9}$. Refined room-temperature lattice parameters are, respectively, 8.611(9) Å for the *a*-axis and 19.40(5) Å for the *c*-axis. First-principles calculations indicate that both Fe^{2+}(tepa) and Fe^{3+}(tepa) complexes are stable, and calculated thickness and diameter are 3.43 and 6.19 Å for Fe^{2+}(tepa) and 4.40 and 7.13 Å for Fe^{3+}(tepa), well matching with the layered structure of $Fe_{14}Se_{16}(tepa)$.[24] In contrast to lattice constants of $Fe_{14}Se_{16}(tepa)_{III,3}$ and $Fe_{14}Se_{16}(tepa)_{III,12}$ (Fig. S5 in the supplementary material), the *a* value changes little, whereas the *c* value obviously shrinks ~6.8% for $Fe_{14}Se_{16}(tepa)_{III,3}$, ~6.9% for $Fe_{14}Se_{16}(tepa)_{III,9}$, and $Fe_{14}Se_{16}(tepa)_{III,12}$, respectively, revealing a slight change of a hybrid structure with prolonging *t*. Figure 2(b) shows *in situ* high-temperature XRD patterns of $Fe_{14}Se_{16}(tepa)_{III,9}$ recorded between 300 and 550 K. No obvious changes in terms of the peak intensity, position, and peak numbers indicate that the hybrid material maintains the original lattice upon heating. However, above 550 K, new XRD peaks at $2\theta = 33.0°$, 43.4°, and 50.6° reveal a structural change of the hybrid nanoplates. Meanwhile, a part of $Fe_{14}Se_{16}(tepa)_{III,9}$ nanoplates decompose, resulting in decomposition products of monoclinic Fe_3Se_4 and hexagonal Fe_7Se_8 [Fig. 2(c)].

Mössbauer spectroscopy is an effective tool to probe the distribution, valence, and spin states of irons and is helpful for

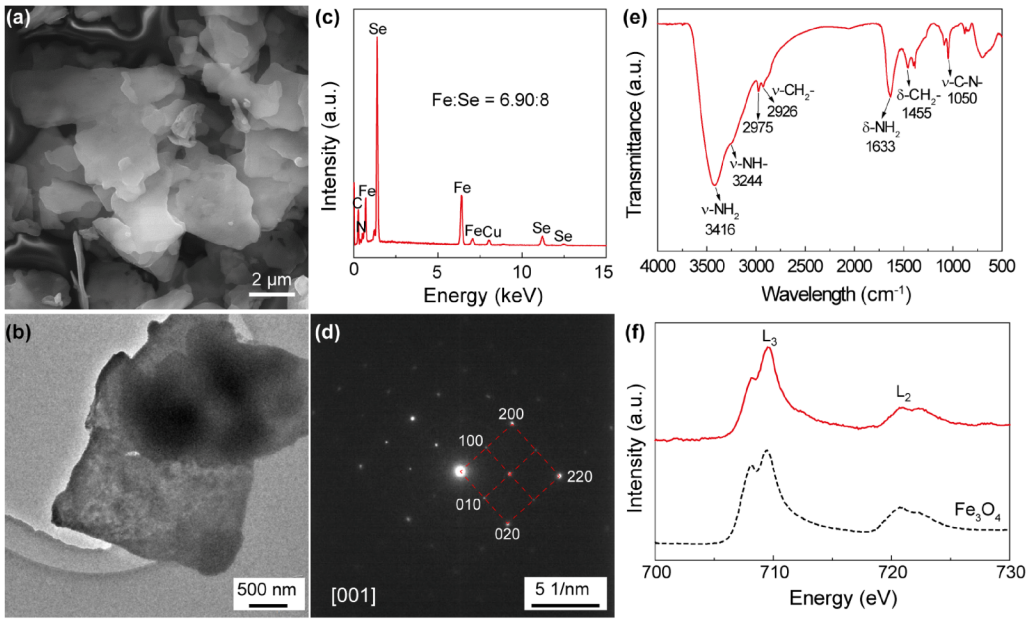

FIG. 1. (a) FESEM image, (b) TEM image, (c) EDX spectrum of the $Fe_{14}Se_{16}(tepa)_{III,9}$ hybrid nanoplates, (d) a corresponding SAED pattern collected perpendicular to the surface of a single hybrid nanoplate in (b), and (e) an FTIR spectrum of the $Fe_{14}Se_{16}(tepa)_{III,9}$ hybrid nanoplates. (f) Fe L-edge XAS spectrum of $Fe_{14}Se_{16}(tepa)_{III,9}$ recorded at room temperature with commercial Fe_3O_4 as a reference.

determining the magnetic ordering of a magnetic material. Figure 3 gives a ^{57}Fe Mössbauer spectrum of $Fe_{14}Se_{16}(tepa)_{III,9}$ recorded at 5 K, exhibiting magnetically splitting sextets in a velocity range between −12 and 12 mm s^{-1}. Based on an FIM model for $Fe_{14}Se_{16}(tepa)_{III,9}$, the ^{57}Fe Mössbauer spectrum was fitted with five magnetically splitting sextets and one non-magnetic doublet. Fit Mössbauer parameters are summarized in Table I. The magnetically splitting sextets could be, respectively, explained by different

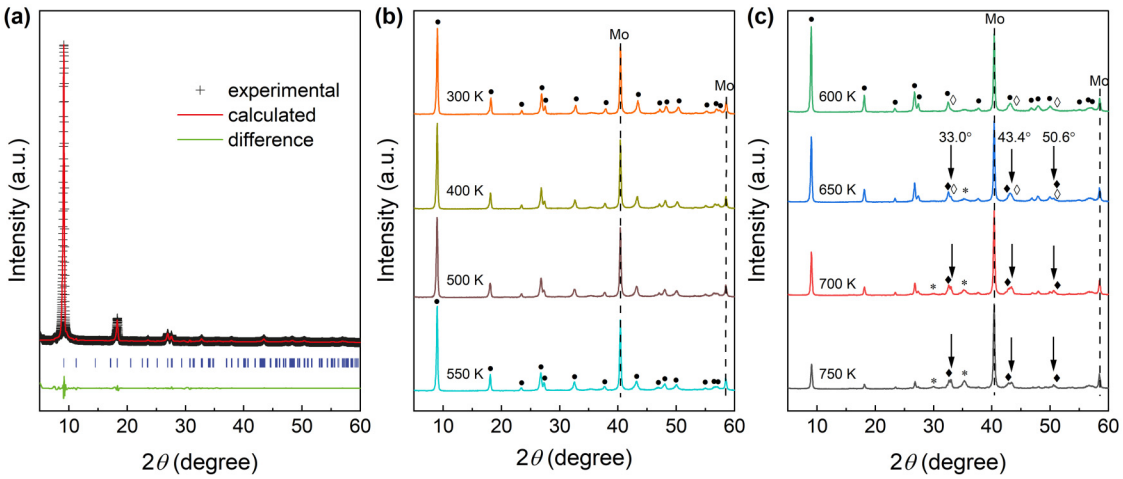

FIG. 2. (a) Slow scanning XRD of $Fe_{14}Se_{16}(tepa)_{III,9}$ recorded at room temperature (solid crosses) with Rietveld refinements and difference curves. *In situ* high-temperature XRD patterns of $Fe_{14}Se_{16}(tepa)_{III,9}$ (●) recorded in a temperature range of (b) 300–550 and (c) 600–750 K. Monoclinic Fe_3Se_4 (◇), hexagonal Fe_7Se_8 (◆), and Fe_3O_4 (*) were gradually formed by thermal decomposition or oxidation at a temperature higher than 550 K.

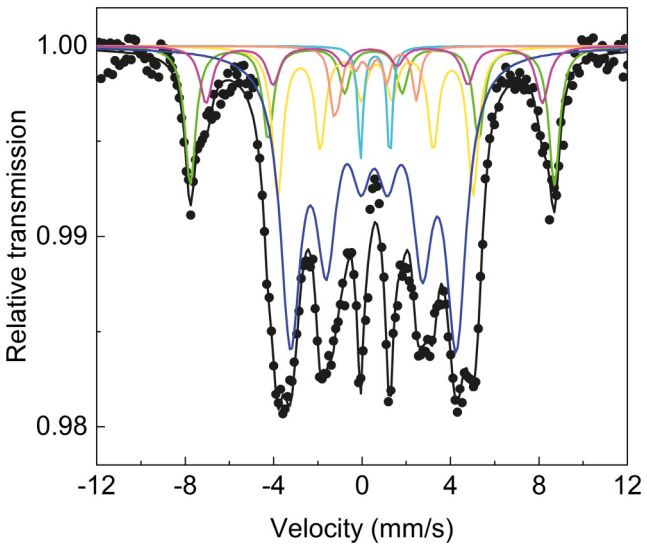

FIG. 3. ^{57}Fe Mössbauer spectrum of $Fe_{14}Se_{16}(tepa)_{III,9}$ collected at 5 K. Experimental data (black dot) and the calculated spectrum (black line) fitted by Fe^{3+} components [green ($S = 5/2$), purple ($S = 5/2$), pink ($S = 1/2$), and cyan ($S = 5/2$)] and Fe^{2+} components [yellow ($S = 2$) and blue ($S = 2$)], respectively. The spin states of irons are shown in parentheses, while the different colored lines represent magnetically nonequivalent sites of Fe^{2+} and Fe^{3+} ions in the hybrid.

magnetic iron sites in β-Fe_3Se_4 layers and spacer layers, while the non-magnetic doublet corresponds to paramagnetic (PM) irons in the Fe(tepa) complexes.[18,37] The hyperfine fields of 275 kOe (yellow) and 232 kOe (blue) are attributed to high-spin Fe^{2+} ($S = 2$) with the isomer shift values of 0.63 and 0.53 mm s^{-1}, respectively. The isomer shifts are remarkably larger than 0.4 mm s^{-1}, excluding the presence of Fe^{3+} ($S = 3/2$) ions.[37,38] The isomer shifts of 0.49 mm s^{-1} (green) and 0.47 mm s^{-1} (purple) are the typical values for high-spin Fe^{3+} ($S = 5/2$), which are supported by corresponding high hyperfine fields of 512 and 473 kOe, respectively. Such high-spin Fe^{3+} ions were never found in the previously reported binary Fe–Se compounds and those containing Fe_xSe fragments, such as Fe_7Se_8,[39] $(FeSe_2)_2[Fe(en)_2]$,[37] Fe_3Se_4,[40] $BaFe_2Se_3$,[41] FeSe,[42] and FeSe-based superconductors.[43,44] However, the high hyperfine fields are well found in the *A* and *B* sites of Fe_3O_4.[45] A molar ratio of Fe^{3+} and Fe^{2+} ions is determined to be 1:2.496 (Table I), the same as the calculated value of 1:2.5 according to the proposed chemical formula of $(Fe^{2+}_{2.5}Fe^{3+}_{0.5}Se^{2-}_4)_4[Fe^{3+}(tepa)]Fe^{3+}$. Such a molar ratio of Fe^{3+} and Fe^{2+} ions is much different from that of 2:1 for Fe_3O_4, excluding the presence of considerable Fe_3O_4 in the hybrid sample. Therefore, the magnetic properties of the hybrids are contributed by the main phase $Fe_{14}Se_{16}(tepa)_{III,9}$ but not a tiny Fe_3O_4 impurity. Moreover, a magnetically splitting sextet (pink) exhibits a hyperfine field of 117 kOe, which is about twice larger than that (66 kOe) of Fe^{2+} ($S = 2$) in the $[Fe^{2+}(en)_2]$ complexes.[37] The isomer shift value of 0.30 mm s^{-1} assigns the pink component to low-spin Fe^{3+} ions in Fe^{3+}(tepa) organic complexes. The isomer shifts of 0.60 mm s^{-1} (cyan) are the typical value for high-spin Fe^{3+} ($S = 5/2$). However, the non-magnetic doublet (~2.9%) of the cyan component suggests that these Fe^{3+} ($S = 5/2$) are PM irons due to coordination with tepa molecules,[37] which is supported by the high quadrupole splitting value of 1.32 mm s^{-1} due to five-coordination of a Fe^{3+}(tepa) complex.[46] Table I reveals that there are ~13.9% interlayer Fe^{3+} ions in spacer layers and ~14.7% high-spin Fe^{3+} and ~71.4% high-spin Fe^{2+} in inorganic Fe_3Se_4 layers. It gives a molar ratio of ~4.9:1 for Fe^{2+}/Fe^{3+} in the inorganic layers, similar to the value of 5:1 determined by the electrical neutrality principles. Considering a similar feature of Fe^{2+}(tepa) and Fe^{3+}(tepa) complexes, we also tried to fit the Mössbauer spectrum assuming the presence of both Fe^{3+}(tepa) and Fe^{2+}(tepa) complexes in $Fe_{14}Se_{16}(tepa)_{III,9}$. However, no non-magnetic Fe^{2+} ($S = 0$ and/or 1) components were resolved out because a significant smaller isomer shift (<0.6 mm s^{-1}) is expected.[38] As a result, in contrast to all interlayer Fe^{2+} in organic layers of $Fe_{14}Se_{16}(tepa)_{II,9}$,[24] the present data confirm that all interlayer iron atoms in $Fe_{14}Se_{16}(tepa)_{III,9}$ have been replaced by high-spin Fe^{3+}.

A field dependence of magnetization in Fig. 4(a) exhibits ferrimagnetism of $Fe_{14}Se_{16}(tepa)_{III,9}$ in the 10–500 K temperature range. The M_S is 9.2 emu g^{-1} at 10 K, which gradually decreases to 7.2 emu g^{-1} at 300 K and 5.9 emu g^{-1} at 500 K, respectively. Temperature dependence of ZFC/FC magnetizations in Fig. 4(b) presents a broad magnetization peak around 90 K in the ZFC magnetization curve recorded at a magnetic field of 0.1 kOe and an obvious divergence between the ZFC/FC magnetization curves at ~110 K. As the applied magnetic field is set to 50 kOe, the ZFC

TABLE I. Summary of the fit parameters for the Mössbauer spectrum of $Fe_{14}Se_{16}(tepa)_{III,9}$ collected at 5 K. An isomer shift (IS), quadrupole splitting (QS), hyperfine magnetic field (HF), linewidth (Γ), and intensity (I) are given.

	IS	QS	Γ	HF			I		
Line		mm s^{-1}		kOe	Fe ion	Spin state	%	Layer	Fe^{3+}/Fe^{2+}
Green	0.49	−0.050	0.59	512	Fe^{3+}	$S = 5/2$	14.7	Fe_3Se_4	1/2.50
Purple	0.47	0.171	0.68	473	Fe^{3+}	$S = 5/2$	7.0	Spacer layer	
Pink	0.30	0.550	0.41	117	Fe^{3+}	$S = 1/2$	4.0		
Cyan	0.60	1.323	0.29	…	Fe^{3+}	$S = 5/2$	2.9		
Yellow	0.63	−0.058	0.59	275	Fe^{2+}	$S = 2$	15.6	Fe_3Se_4	
Blue	0.53	−0.042	1.12	233	Fe^{2+}	$S = 2$	55.8		

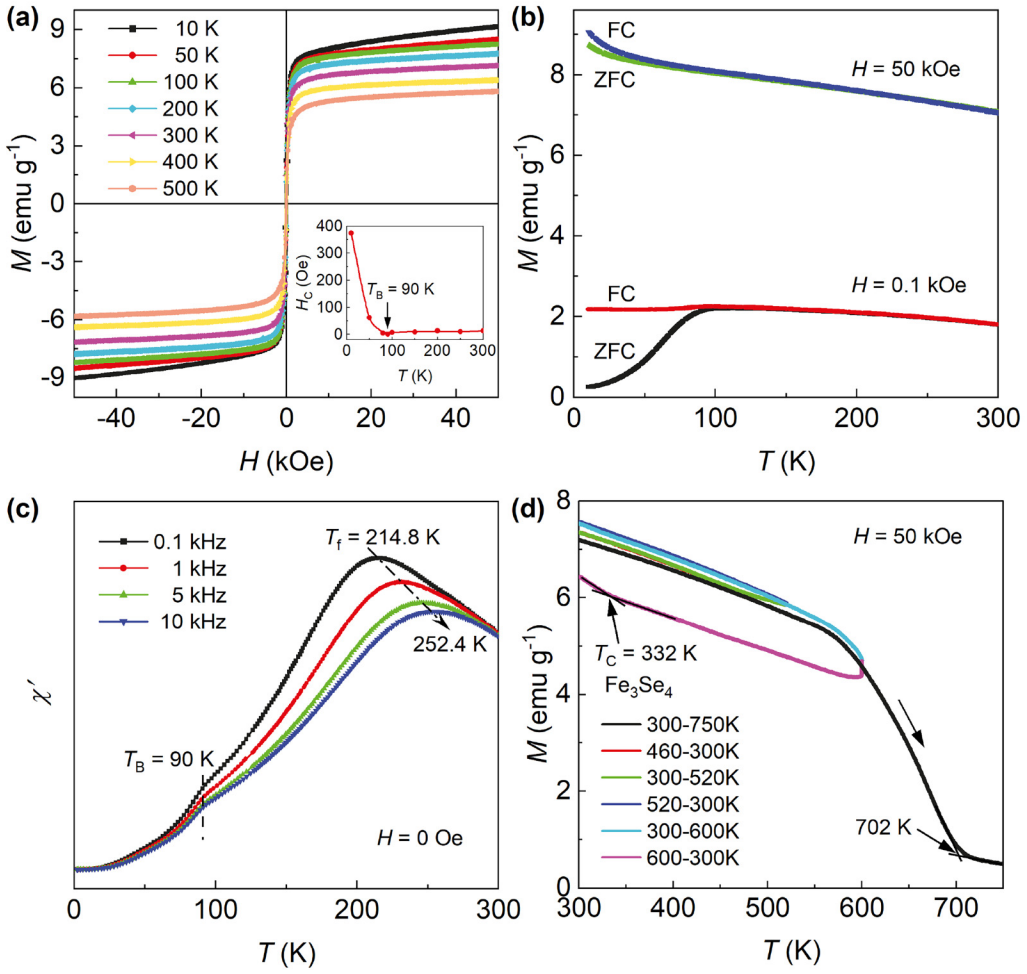

FIG. 4. Magnetic properties of $Fe_{14}Se_{16}(tepa)_{III,9}$. (a) Magnetic hysteresis loops were recorded between −50 and 50 kOe in the 10–500 K temperature range. The inset shows an obvious decrease of H_C with increasing the temperature from 10 to 90 K. The red line guides the eyes. (b) Temperature dependence of ZFC and FC magnetizations under an applied magnetic field of 0.1 and 50 kOe in the 10–300 K temperature range. (c) Temperature dependence of ac susceptibility χ' collected at zero magnetic field and different frequencies. (d) Temperature dependence of magnetization at a magnetic field of 50 kOe measured in a heating process from 300 to 750 K and different heating/cooling processes in the 300–460, the 300–520, and the 300–600 K range, respectively.

magnetization peak disappears. The ZFC/FC magnetization curves dependent on an applied magnetic field are characteristic of the spin-glass state[47] or superparamagnetism,[48] distinguishing them from general thermodynamic phase transitions. To determine an origin of the ZFC magnetization peak, a temperature dependence of ac susceptibility was measured at a zero magnetic field and different frequencies [Fig. 4(c)]. The in-phase components χ' appear two wide peaks at 80–110 and 210–260 K temperature ranges, respectively. The χ' peak at lower temperatures is independent of the frequencies, which should be ascribed to the superparamagnetic behavior with a blocking temperature (T_B) of ~90 K. The superparamagnetism is supported by a change of coercivity (H_C) shown as the inset of Fig. 4(a), where the H_C values sharply drop from 380 Oe at 10 K to ~8 Oe at 90 K. Previously, the critical radius for a single-domain monoclinic Fe_3Se_4 particle is about 800 nm at 10 K and about 2000 nm at 300 K, respectively.[58] Non-zero H_C values above 90 K reveal the presence of a small amount of multidomain hybrid particles in $Fe_{14}Se_{16}(tepa)_{III,9}$.[48,49] The peak in the higher temperature range exhibits a peak temperature shifting from 214.8 to 252.4 K as the frequency increases from 0.1 to 10 kHz, clarifying a spin-glass state in $Fe_{14}Se_{16}(tepa)_{III,9}$. Spin-glass is in short-range magnetic orders, which are usually observed in frustrated magnetic systems. The theoretical article[50] proved that a long-range magnetic order can coexist with a spin-glass disorder in a magnetic material. Magnetically splitting sextets in Fig. 3 reveal 3D long-range magnetic ordering in the hybrid ferrimagnet, whereas the frustrated spins in local environments, such as interface and boundaries, are in the spin-glass state. Due to a tiny minority of ~2.9%

TABLE II. Magnetic moments and energy per formula for five possible spin configurations of $(Fe^{2+}_{2.5}Fe^{3+}_{0.5}Se^{2-}_{4})_4[Fe^{3+}(tepa)]Fe^{3+}$. Fe1 and Fe2 are interlayer iron, Fe1 located at the 2*a* site and Fe2 located at the 2*b* site; NM, nonmagnetic; FM, ferromagnetic; ↑, spin up; and ↓, spin down.

Type	Fe1	Fe2	Fe1 (μ_B)	Fe2 (μ_B)	Fe1 + Fe2 (μ_B)	Fe_3Se_4 (μ_B)	Total (μ_B)	Energy (eV)
NM	NM	NM	−2.835	3.694	0.859	0.052	0.911	−143.362
FM-1	NM	FM↑	−3.265	3.376	0.111	0.064	0.175	−143.381
FM-2	FM↑	NM	3.059	3.390	6.449	−0.46	5.989	−142.960
FM-3	FM↑	FM↑	3.178	3.506	6.684	0.114	6.798	−143.412
FM-4	FM↑	FM↓	3.285	−3.379	−0.094	−0.256	−0.35	−143.274

non-magnetic irons at 5 K (Table I), there is a negligible effect of frustrated irons on the magnetizations of $Fe_{14}Se_{16}(tepa)_{III,9}$.

A high-temperature thermal magnetization (M–T) curve of $Fe_{14}Se_{16}(tepa)_{III,9}$ in Fig. 4(d) illustrates that the highest T_N of $Fe_{14}Se_{16}(tepa)_{III,9}$ approaches 702 K corresponding to the disappearance of FIM order of $Fe_{14}Se_{16}(tepa)_{III,9}$. This temperature is much higher than that (683 K) of $Fe_{14}Se_{16}(tepa)_{II,9}$ (Fig. S6 in the supplementary material) due to substitution of Fe^{3+} for Fe^{2+} in the organic spacer layers. Because all iron selenides in the decomposed product are paramagnetic above 460 K,[39,40] a small magnetization of ∼0.5 emu/g at 50 kOe and 750 K suggests that tiny inclusion of Fe_3O_4 nanoparticles could not dominate the magnetic properties of nanoplates [Figs. 4(a) and 4(b)]. Temperature dependence of magnetization of $Fe_{14}Se_{16}(tepa)_{III,9}$ was also measured in different heating/cooling processes in 300–460, 300–520, and 300–600 K ranges, respectively [Fig. 4(d)]. Compared to the magnetizations in an initial heating process, the M slightly increases in cooling processes from 460 to 300 K and from 520 to 300 K due to improved crystallization and/or removing adsorbed organic molecules on surfaces of hybrid nanoplates. However, a decomposition of $Fe_{14}Se_{16}(tepa)_{III,9}$ above T_d (560 K) leads to not only a decrease of magnetization but also an irreversible change between heating and cooling magnetization curves. A cooling process from 600 to 300 K shows a magnetic transition at ∼332 K originating from a decomposition product of Fe_3Se_4[51] as revealed in Fig. 2(c). Therefore, a defined T_N value of $Fe_{14}Se_{16}(tepa)_{III,9}$ is hardly determined because the hybrid phase initially decomposes prior to the FIM–PM transition of $Fe_{14}Se_{16}(tepa)_{III,9}$. At least, the T_N of $Fe_{14}Se_{16}(tepa)_{III,9}$ is equivalent to the FIM ordering temperature (∼560 K) of the "garnet" ferrimagnets of $R_3Fe_5O_{12}$ (R = Y, Gd, Dy, and Ho).[52] A recorded high T_N value of $Fe_{14}Se_{16}(tepa)_{III,9}$ is significantly better than any known Fe–Se binary compounds[39,51,53–56] and organic–inorganic hybrid magnets.[17] Moreover, $Fe_{14}Se_{16}(tepa)_{III,9}$ shows higher thermal stability than the popular rare-earth-free permanent magnet of α''-$Fe_{16}N_2$ with a $T_d \sim 510$ K.[57] Excellent thermal stability and magnetic properties make $Fe_{14}Se_{16}(tepa)_{III,9}$ potential in room-temperature magnetic applications.

Usually, tetragonal β-Fe_3Se_4 is in an AFM ground state,[22,30] which was used to synthesize a $(Fe_3Se_4)_4[Fe^{2+}(tepa)]_{0.8}Fe^{2+}_{1.2}$ superconductor with a superconducting critical transition temperature of ∼42 K.[24] High-temperature superconductivity of the hybrid superconductor originates from complete suppression of FIM order in $Fe_{14}Se_{16}(tepa)_{II}$ by removing 0.2 tepa/unit cell. Thus, the 3D long-range magnetic ordering in $Fe_{14}Se_{16}(tepa)_{III,9}$ is dependent magnetic interactions between interlayer and intralayer irons. Similar to $(NH_3)Fe_{0.25}Fe_2S_2$,[34] here, we discuss an origin of the strong ferrimagnetism based on first-principles calculations. Initially, the intralayer Fe atoms in inorganic β-Fe_3Se_4 layers were assigned AFM spin configurations similar to those found in $AFe_{1.5}Se_2$ (A = K, Rb, Cs, or Tl).[30] Under symmetry constraints, we considered five possible spin configurations of interlayer irons as follows: NM (where both Fe1 and Fe2 are nonmagnetic), FM-1 (where Fe1 is nonmagnetic and Fe2 is spin up), FM-2 (where Fe1 is spin up and Fe2 is nonmagnetic), FM-3 (where both Fe1 and Fe2 have the same spin orientation), and FM-4 (where Fe1 is spin up and Fe2 have the opposite spin orientation). The calculated energy and atomic magnetic moments after relaxation calculations are summarized in Table II.

Considering that the saturation magnetization of $Fe_{14}Se_{16}(tepa)_{III,9}$ at 10 K is 3.68 μ_B, the results of simulated FM-2 and FM-3 spin configurations are closest to the experimental value. The calculations predict that the FM-3 has the lowest total energy, while the FM-2 has the highest total energy (see Table II). The calculated energy differences between them are small ($\Delta < 0.5$ eV) since only the possible spin orientations of two interstitial Fe atoms are studied here, given that the Fe_3Se_4 layer is in an AFM order. The exchange parameters of FeSe-based compounds have been reported in the order of magnitude of mRy;[58,59] thus, the energy difference can be derived in the order of magnitude of 0.1 eV when the spins of interstitial Fe1 and Fe2 are flipped, roughly in agreement with the calculated results. To a certain degree, the FM-3 is the most likely choice for the atomic magnetic moments of interlayer Fe1 and Fe2 in $Fe_{14}Se_{16}(tepa)_{III,9}$. The magnetism mainly originates from the interlayer Fe atoms, similar to the cases of $Li_{1-x}Fe_xOHFeSe$[60,61] and $(NH_3)Fe_{0.25}Fe_2S_2$.[34] It is important to note that the spin configuration of the intralayer Fe in the Fe_3Se_4 layer of the FM-3 is initially antiferromagnetic while contributing a small net magnetic moment after optimized relaxation. It is possible that intralayer high-spin Fe^{3+} in a Fe_6Se_8 layer of $(Fe^{2+}_{2.5}Fe^{3+}_{0.5}Se^{2-}_{4})_4[Fe^{3+}(tepa)]Fe^{3+}$ cannot be canceled out by high-spin Fe^{2+}. As a result, spin configuration of intralayer irons unequivocally changes from an AFM ground state to a FIM order. In contrast to $Fe_{14}Se_{16}(tepa)_{II,9}$,[24] introduction of high-spin Fe^{3+} into the spacer layers is responsible to enhance intra- and interlayer magnetic interactions and, thus, an increase in ferrimagnetism of $Fe_{14}Se_{16}(tepa)_{III,9}$.

IV. CONCLUSION

The organic–inorganic $Fe_{14}Se_{16}(tepa)_{III,9}$ magnetic nanoplates are constructed by self-assembly of β-Fe_3Se_4 layers and spacing

layers involving tepa-coordinated and uncoordinated Fe^{3+} ions. Both interlayer and intralayer high-spin irons are well integral to 3D long-range AFM coupling that creates the strong ferrimagnetism in $Fe_{14}Se_{16}(tepa)_{III,9}$. The striking high-temperature magnetic properties (the M_S value is 5.9 emu g^{-1} at 500 K) and the record-high Néel temperature ($T_N > 560$ K) make $Fe_{14}Se_{16}(tepa)_{III,9}$ substantially superior to the previously reported organic magnets and all of the inorganic Fe_xSe counterparts. As a new category of organic magnets, ordered organic–inorganic $Fe_{14}Se_{16}(tepa)_{II/III}$ provides a platform to create a wider range of analogous magnets for a strong magnetism and, thus, interesting multi-functionality due to flexible hybrid structures and controllable spin states of irons.

SUPPLEMENTARY MATERIAL

Experimental conditions for synthesis of hybrid materials are shown in Table S1 of the supplementary material. Figures S1–S6 include SEM, TEM, EDX, TGA, dMass/d*T*, XRD, and magnetic data of hybrid materials. Experimental details are for determination of the molar ratio between an inorganic component (Fe_7Se_8) and tepa.

ACKNOWLEDGMENTS

This work was supported by the National Key R&D Program of China (Nos. 2023YFB3507601 and 2022YFA1203901), the Ministry of Science and Technology of China, and the National Natural Science Foundation of China (NSFC) (Nos. 52371203, 52031014, and 51971221). B.D. acknowledges the support from NSFC with Nos. 12004228 and U21A6004. The authors acknowledge the Beamline BL08U1A station of the Shanghai Synchrotron Radiation Facility (SSRF) for XAS measurements.

AUTHOR DECLARATIONS

Conflict of Interest

The authors have no conflicts to disclose.

Author Contributions

D.L. and **Z.Z.** conceived the experiments and supervised the overall project. **Q.K. and X.M.** fabricated the samples. **Q.K., B.Z., Y.Z., B.Y., Z.L., and X.S.** performed experimental measurements. **J.H., B.D.,** and **T.Y.** conducted the theoretical simulations. The manuscript was written by **Q.K.**, **D.L.,** and **Z.Z.** with discussion and inputs from all the authors.

Qifeng Kuang: Conceptualization (equal); Data curation (equal); Investigation (equal); Writing – original draft (equal). **Bo Zhang:** Investigation (equal). **Baojuan Dong:** Funding acquisition (equal); Investigation (equal). **Xiaoling Men:** Investigation (equal); Methodology (equal). **Bing Yang:** Investigation (equal). **Yangtao Zhou:** Investigation (equal). **Zhiwei Li:** Methodology (equal). **Xiaolei Shang:** Data curation (equal); Investigation (equal). **Teng Yang:** Methodology (equal). **Jianqi Huang:** Methodology (equal); Writing – review & editing (equal). **Da Li:** Conceptualization (equal); Funding acquisition (equal); Project administration (equal); Resources (equal); Supervision (equal); Writing – review & editing (equal). **Zhidong Zhang:** Funding acquisition (equal); Supervision (equal); Writing – review & editing (equal).

DATA AVAILABILITY

The datasets generated during and/or analyzed during the current study are available from the corresponding author upon reasonable request.

REFERENCES

[1]M. Clemente-León, E. Coronado, C. Martí-Gastaldo, and F. M. Romero, Chem. Soc. Rev. **40**(2), 473–497 (2011).
[2]Y. Ma, Y. Wang, J. Cong, and Y. Sun, Phys. Rev. Lett. **122**(25), 255701 (2019).
[3]H. Liu, C. Zhang, H. Malissa, M. Groesbeck, M. Kavand, R. McLaughlin, S. Jamali, J. Hao, D. Sun, R. A. Davidson, L. Wojcik, J. S. Miller, C. Boehme, and Z. V. Vardeny, Nat. Mater. **17**(4), 308–312 (2018).
[4]B. Nafradi, P. Szirmai, M. Spina, H. Lee, O. V. Yazyev, A. Arakcheeva, D. Chernyshov, M. Gibert, L. Forro, and E. Horvath, Nat. Commun. **7**, 13406–13414 (2016).
[5]M. Wei, K. Song, Y. Yang, Q. Huang, Y. Tian, X. Hao, and W. Qin, Adv. Mater. **32**(40), 2003293 (2020).
[6]J. M. Manriquez, G. T. Yee, R. S. Mclean, A. J. Epstein, and J. S. Miller, Science **252**(5011), 1415–1417 (1991).
[7]S. Ferlay, T. Mallah, R. Ouahes, P. Veillet, and M. Verdaguer, Nature **378**(6558), 701–703 (1995).
[8]Ø. Hatlevik, W. E. Buschmann, J. Zhang, J. L. Manson, and J. S. Miller, Adv. Mater. **11**(11), 914–918 (1999).
[9]K. S. Pedersen, P. Perlepe, M. L. Aubrey, D. N. Woodruff, S. E. Reyes-Lillo, A. Reinholdt, L. Voigt, Z. Li, K. Borup, M. Rouzières, D. Samohvalov, F. Wilhelm, A. Rogalev, J. B. Neaton, J. R. Long, and R. Clérac, Nat. Chem. **10**(10), 1056–1061 (2018).
[10]P. Perlepe, I. Oyarzabal, A. Mailman, M. Yquel, M. Platunov, I. Dovgaliuk, M. Rouzieres, P. Negrier, D. Mondieig, E. A. Suturina, M. A. Dourges, S. Bonhommeau, R. A. Musgrave, K. S. Pedersen, D. Chernyshov, F. Wilhelm, A. Rogalev, C. Mathoniere, and R. Clerac, Science **370**(6516), 587–592 (2020).
[11]P. Judeinstein and C. Sanchez, J. Mater. Chem. **6**(4), 511–525 (1996).
[12]C. N. R. Rao, A. K. Cheetham, and A. Thirumurugan, J. Phys.: Condens. Matter **20**(8), 083202 (2008).
[13]P. Rabu and M. Drillon, Adv. Eng. Mater. **5**(4), 189–210 (2003).
[14]Z. Wang, K. Hu, S. Gao, and H. Kobayashi, Adv. Mater. **22**(13), 1526–1533 (2010).
[15]Y.-Z. Zheng, W. Xue, S.-L. Zheng, M.-L. Tong, and X.-M. Chen, Adv. Mater. **20**(8), 1534–1538 (2008).
[16]S. M. Holmes and G. S. Girolami, J. Am. Chem. Soc. **121**(23), 5593–5594 (1999).
[17]D. Pan, Y. Li, Z. Han, B. Li, C. Wang, T. Yang, D. Li, C. Choi, and Z. Zhang, Chem. Mater. **30**(24), 8975–8982 (2018).
[18]D. Pan, Q. Kuang, P. Tong, W. Tong, L. Fan, J. Zhao, D. Li, C. Choi, and Z. Zhang, J. Magn. Magn. Mater. **542**, 168585 (2022).
[19]D. Tiana, C. H. Hendon, and A. Walsh, Chem. Commun. **50**(90), 13990–13993 (2014).
[20]J. Lopez-Cabrelles, S. Manas-Valero, I. J. Vitorica-Yrezabal, M. Siskins, M. Lee, P. G. Steeneken, H. S. J. van der Zant, G. M. Espallargas, and E. Coronado, J. Am. Chem. Soc. **143**(44), 18502–18510 (2021).
[21]J. T. Greenfield, C. Pak, S. Kamali, K. Lee, and K. Kovnir, Chem. Commun. **51**(25), 5355–5358 (2015).
[22]Q. Kuang, X. Men, X. Shang, B. Yang, Y. Zhou, B. Zhang, Z. Li, D. Li, and Z. Zhang, Magnetism **2**(1), 31–44 (2022).
[23]X. Shang, X. Men, Q. Kuang, S. Li, D. Li, and Z. Zhang, Nanomaterials **13**(3), 487 (2023).
[24]D. Li, Q. Kuang, X. Men, B. Zhang, J. Huang, X. Shang, B. Yang, T. Yang, Z. Li, and Z. Zhang, J. Mater. Sci. Technol. **198**, 98–110 (2024).

[25]G. Kresse and J. Furthmuller, Phys. Rev. B **54**(16), 11169–11186 (1996).
[26]G. Kresse and J. Furthmuller, Comput. Mater. Sci. **6**(1), 15–50 (1996).
[27]P. E. Blochl, Phys. Rev. B **50**(24), 17953–17979 (1994).
[28]H. J. Monkhorst and J. D. Pack, Phys. Rev. B **13**(12), 5188–5192 (1976).
[29]T. K. Chen, C. C. Chang, H. H. Chang, A. H. Fang, C. H. Wang, W. H. Chao, C. M. Tseng, Y. C. Lee, Y. R. Wu, M. H. Wen, H. Y. Tang, F. R. Chen, M. J. Wang, M. K. Wu, and D. Van Dyck, Proc. Natl. Acad. Sci. U.S.A. **111**(1), 63–68 (2014).
[30]X.-W. Yan, M. Gao, Z.-Y. Lu, and T. Xiang, Phys. Rev. Lett. **106**(8), 087005 (2011).
[31]D. Li, D. S. Pan, W. L. Liu, X. X. Li, M. L. Chen, S. J. Li, Y. Li, J. Tan, D. M. Sun, Z. H. Wang, Z. Han, and Z. D. Zhang, Chem. Mater. **29**(2), 842–848 (2017).
[32]W. Bao, Q.-Z. Huang, G.-F. Chen, M.-A. Green, D.-M. Wang, J.-B. He, and Y.-M. Qiu, Chin. Phys. Lett. **28**(8), 086104 (2011).
[33]M. Burrard-Lucas, D. G. Free, S. J. Sedlmaier, J. D. Wright, S. J. Cassidy, Y. Hara, A. J. Corkett, T. Lancaster, P. J. Baker, S. J. Blundell, and S. J. Clarke, Nat. Mater. **12**(1), 15–19 (2013).
[34]X. Lai, Z. Lin, K. Bu, X. Wang, H. Zhang, D. Li, Y. Wang, Y. Gu, J. Lin, and F. Huang, RSC Adv. **6**(85), 81886–81893 (2016).
[35]A. Zhang, T. Xia, K. Liu, W. Tong, Z. Yang, and Q. Zhang, Sci. Rep. **3**(1), 1216 (2013).
[36]C. Dong, J. Appl. Crystallogr. **32**, 838 (1999).
[37]C. Pak, S. Kamali, J. Pham, K. Lee, J. T. Greenfield, and K. Kovnir, J. Am. Chem. Soc. **135**(51), 19111–19114 (2013).
[38]P. Gütlich and J. Ensling, *Handbook of Analytical Techniques* (John Wiley & Sons, Ltd., 2001), pp. 561–577.
[39]H. N. Ok and S. W. Lee, Phys. Rev. B **8**(9), 4267–4269 (1973).
[40]R. Pohjonen, O. Mustonen, M. Karppinen, and J. Lindén, J. Alloys Compd. **746**, 135–139 (2018).
[41]M. Reissner, W. Steiner, and H. Boller, in *^{57}Fe Mössbauer Studies on $BaFe_2X_3$ Compounds with $X = S$, Se* (Springer Netherlands, Dordrecht, 2002), pp. 197–200.
[42]A. Blachowski, K. Ruebenbauer, J. Zukrowski, J. Przewoznik, K. Wojciechowski, and Z. M. Stadnik, J. Alloys Compd. **494**(1–2), 1–4 (2010).
[43]D. H. Ryan, W. N. Rowan-Weetaluktuk, J. M. Cadogan, R. Hu, W. E. Straszheim, S. L. Bud'ko, and P. C. Canfield, Phys. Rev. B **83**(10), 104526 (2011).
[44]S. I. Shylin, V. Ksenofontov, S. J. Sedlmaier, S. J. Clarke, S. J. Cassidy, G. Wortmann, S. A. Medvedev, and C. Felser, Europhys. Lett. **109**(6), 67004 (2015).
[45]B. J. Evans and S. S. Hafner, J. Appl. Phys. **40**(3), 1411–1413 (1969).
[46]G. Roelfes, V. Vrajmasu, K. Chen, R. Y. N. Ho, J.-U. Rohde, C. Zondervan, R. M. la Crois, E. P. Schudde, M. Lutz, A. L. Spek, R. Hage, B. L. Feringa, E. Münck, and L. Que, Inorg. Chem. **42**(8), 2639–2653 (2003).
[47]Z. Zhang, J. Mater. Sci. Technol. **44**, 116–120 (2020).
[48]X. X. Zhang, J. M. Hernàndez, J. Tejada, R. Solé, and X. Ruiz, Phys. Rev. B **53**(6), 3336–3340 (1996).
[49]Z. D. Zhang, J. L. Yu, J. G. Zheng, I. Skorvanek, J. Kovac, X. L. Dong, Z. J. Li, S. R. Jin, H. C. Yang, Z. J. Guo, W. Liu, and X. G. Zhao, Phys. Rev. B **64**(2), 024404 (2001).
[50]M. Gabay and G. Toulouse, Phys. Rev. Lett. **47**(3), 201–204 (1981).
[51]A. F. Andresen and B. V. Laar, Acta Chem. Scand. **24**(7), 2435–2439 (1970).
[52]G. C. Papaefthymiou, *Nanomagnetism: An Interdisciplinary Approach* (Chapman & Hall/CRC, New York, 2022).
[53]I. S. Lyubutin, C.-R. Lin, K. O. Funtov, T. V. Dmitrieva, S. S. Starchikov, Y.-J. Siao, and M.-L. Chen, J. Chem. Phys. **141**(4), 044704 (2014).
[54]F.-C. Hsu, J.-Y. Luo, K.-W. Yeh, T.-K. Chen, T.-W. Huang, P. M. Wu, Y.-C. Lee, Y.-L. Huang, Y.-Y. Chu, D.-C. Yan, and M.-K. Wu, Proc. Natl. Acad. Sci. U.S.A. **105**(38), 14262–14264 (2008).
[55]X. J. Wu, Z. Z. Zhang, J. Y. Zhang, B. H. Li, Z. G. Ju, Y. M. Lu, B. S. Li, and D. Z. Shen, J. Appl. Phys. **103**(11), 113501 (2008).
[56]H. Zhang, G. Long, D. Li, R. Sabirianov, and H. Zeng, Chem. Mater. **23**(16), 3769–3774 (2011).
[57]Y. Li, Q. Kuang, X. Men, S. Wang, D. Li, C. Choi, and Z. Zhang, Nanomaterials **11**(4), 890 (2021).
[58]G. Long, H. Zhang, D. Li, R. Sabirianov, Z. Zhang, and H. Zeng, Appl. Phys. Lett. **99**(20), 202103 (2011).
[59]F. Ma, W. Ji, J. Hu, Z.-Y. Lu, and T. Xiang, Phys. Rev. Lett. **102**(17), 177003 (2009).
[60]X. F. Lu, N. Z. Wang, H. Wu, Y. P. Wu, D. Zhao, X. Z. Zeng, X. G. Luo, T. Wu, W. Bao, G. H. Zhang, F. Q. Huang, Q. Z. Huang, and X. H. Chen, Nat. Mater. **14**(3), 325–329 (2015).
[61]U. Pachmayr, F. Nitsche, H. Luetkens, S. Kamusella, F. Bruckner, R. Sarkar, H.-H. Klauss, and D. Johrendt, Angew. Chem. Int. Ed. **54**(1), 293–297 (2015).